






The Chemical Signatures of Planetary Engulfment Events in Binary Systems

Tushar Nagar , Lorenzo Spina , and Amanda I. Karakas 

Monash Centre for Astrophysics, School of Physics and Astronomy, Monash University, VIC 3800, Australia; tusharnagar64@gmail.com

Received 2019 August 29; revised 2019 November 7; accepted 2019 November 21; published 2019 December 31

Abstract

Planetary engulfment events involve the chemical assimilation of a planet into a star’s external layer. This can cause a change in the chemical pattern of the stellar atmosphere in a way that mirrors the composition of the rocky object engulfed, with the refractory elements being more abundant than the volatiles. Due to these stellar chemical changes, planetary engulfment events can render the process of chemical tagging potentially inaccurate. A line-by-line differential analysis of twin stars in wide binary systems allows us to test the chemical homogeneity of these associations with typical individual stellar Fe I uncertainties of 0.01 dex and eventually unveil chemical anomalies that could be attributed to planetary engulfment events. Out of the 14 systems analyzed here, we report the discovery of the most chemically inhomogeneous system to date (HIP 34407/HIP 34426). The median difference in abundances of refractory elements within the pair is 0.19 dex and the trend between the differential abundances and condensation temperature suggests that the anomaly is likely due to a planetary engulfment event. Within our sample, five other chemically anomalous systems are found.

Unified Astronomy Thesaurus concepts: [Chemical abundances \(224\)](#); [Stellar abundances \(1577\)](#); [Wide binary stars \(1801\)](#); [Exoplanets \(498\)](#); [Chemically peculiar stars \(226\)](#)

Supporting material: machine-readable tables

1. Introduction

Within the last decade, radial velocity and transit surveys have discovered thousands of exoplanets around Sun-like stars. The global picture that has emerged exhibits a remarkable degree of diversity in terms of the architectures of these planetary systems (Winn & Fabrycky 2015). Presumably, this observed diversity has arisen as a result of dynamical processes acting since the first stage of planetesimal formation (Chambers 2018; Raymond et al. 2018). The fact that some systems have undergone complex phases of dynamical evolution is also attested to by the presence of planets on highly eccentric orbits (e.g., Kane et al. 2012) that are misaligned or even counter rotating with respect to the spin axes of their hosting star (e.g., Naoz et al. 2011), interstellar exoplanets (e.g., Mróz et al. 2018), or by the observation of dusty debris disks formed through exoplanet collisions (e.g., Kenyon & Bromley 2016). It is likely that in systems with evidence of a dynamical past, part of the planetary material has fallen into the hosting star (e.g., Martinez et al. 2019; Liu et al. 2018), polluting its atmosphere and producing a significant increase in the stellar metallicity, which can be reliably detected (e.g., Spina et al. 2015, 2018; Oh et al. 2018; Tucci Maia et al. 2019). In fact, such a dilution will not yield an indiscriminate abundance rise of all the heavy elements, but instead will produce a characteristic chemical pattern that mirrors the composition observed in rocky materials (Chambers 2010; Yana Galarza et al. 2016; Kunitomo et al. 2018) with most refractory elements (e.g., those having condensation temperature $T_{\text{cond}} > 1000$ K) being over-abundant relative to the volatiles ($T_{\text{cond}} < 1000$ K).

Prior proposals to explain these signatures suggest that the anomalous volatile to refractory ratios may be due to the selective accretion of volatiles. This could occur after the formation of rocky planets around a star (Meléndez et al. 2009). However, as already discussed in Spina et al. (2018), this explanation seems unlikely, as the chemical signature would have been imprinted on the star when it was too young

(age ≤ 10 Myr), diluting any accreted material due to the star’s thick external layer.

Unveiling the chemical signatures of planetary engulfment events in stellar atmospheres is key to studying the frequency over which these catastrophic events occur, but it is also relevant to test the chemical homogeneity of stellar associations and probe the success of “chemical tagging.” The concept of chemical tagging is to use the chemical information of stars to assign them to their progenitor cloud (Freeman & Bland-Hawthorn 2002). A critical assumption of this technique is that members of the same stellar associations, such as open clusters or binary systems, are chemically identical as they formed at the same time and from the same material. Therefore, if the abundance of any element is altered due to a planetary engulfment event, the results from chemical tagging will no longer be reflective of the star’s progenitor cloud.

In this Letter we examine the chemical homogeneity of 14 wide binary star systems, making use of high-precision abundance determinations. In Section 2 we describe the target selection, observations, and method of analysis. The results of our study are presented in Section 3 and our conclusions in Section 4.

2. Observations and Analysis

The 28 target stars were selected from lists of wide binary systems (separation $> 4''$) compiled by Martín et al. (2002), Desidera et al. (2004), and Fuhrmann & Chini (2015). Proper motions, radial velocities, and parallaxes from *Gaia* DR2 (Gaia Collaboration et al. 2018) are listed in Table 1 and confirm that the pairs are physical systems. For this project, we have chosen only the pairs formed by twin dwarf stars with spectral types similar to that of the Sun. Twin stars are objects with atmospheric parameters very similar to each other (e.g., $\Delta T_{\text{eff}} \lesssim 300$ K and $\Delta \log g \lesssim 0.2$ dex). It has been shown that a strictly differential line-by-line analysis of twin stars permits us to obtain differential abundances at the highest precision

Table 1
Target Selection

Star	<i>Gaia</i> DR2 Kinematics				S/N	Instrument
	Parallax (mas)	pmRA (mas yr ⁻¹)	pmDEC (mas yr ⁻¹)	Radial velocity (km s ⁻¹)		
Sun						
BD+132311A	6.07 ± 0.05	-56.44 ± 0.08	-41.78 ± 0.06	26.33 ± 1.07	400	UVES
BD+132311B	5.72 ± 0.05	-53.16 ± 0.08	-41.86 ± 0.06	26.08 ± 0.66	300	UVES
HIP 34407	20.97 ± 0.05	-51.63 ± 0.09	-206.35 ± 0.08	-12.64 ± 0.19	300	UVES
HIP 34426	20.87 ± 0.05	-54.18 ± 0.09	-213.07 ± 0.08	-11.83 ± 0.20	350	UVES
HIP 39409A	15.39 ± 0.04	-15.41 ± 0.05	-14.81 ± 0.04	47.78 ± 0.15	300	UVES
HIP 39409B	15.31 ± 0.04	-15.13 ± 0.06	-13.07 ± 0.04	...	400	UVES
HIP 44858	20.45 ± 0.10	-53.24 ± 0.13	71.66 ± 0.10	30.02 ± 0.22	300	UVES
HIP 44864	20.36 ± 0.09	-51.82 ± 0.11	73.52 ± 0.07	30.31 ± 0.14	350	UVES
HIP 47836	17.37 ± 0.04	-23.58 ± 0.07	97.16 ± 0.07	-2.25 ± 0.22	300	UVES
HIP 47839	17.49 ± 0.04	-21.34 ± 0.07	98.41 ± 0.06	-1.94 ± 0.21	300	UVES
HIP 49520A	17.07 ± 0.05	41.09 ± 0.07	-57.17 ± 0.07	-0.56 ± 0.67	300	UVES
HIP 49520B	17.05 ± 0.12	56.91 ± 0.17	-52.46 ± 0.17	1.11 ± 0.45	350	UVES
HIP 58298A	13.16 ± 0.06	35.76 ± 0.09	-65.41 ± 0.04	-3.62 ± 0.27	300	UVES
HIP 58298B	13.06 ± 0.06	37.08 ± 0.10	-71.90 ± 0.04	-3.35 ± 0.29	300	UVES
HR 4443	35.98 ± 0.13	-22.03 ± 0.19	139.98 ± 0.15	7.15 ± 0.53	350	UVES
HR 4444	36.06 ± 0.13	-19.60 ± 0.19	144.52 ± 0.16	...	350	UVES
HD 98744	5.55 ± 0.06	35.39 ± 0.10	-36.02 ± 0.17	...	350	HDS
HD 98745	4.57 ± 0.31	37.54 ± 2.15	-36.15 ± 2.19	...	350	HDS
HD 103431	25.25 ± 0.05	-450.60 ± 0.08	-15.50 ± 0.06	5.76 ± 0.22	400	HDS
HD 103432	25.24 ± 0.05	-450.50 ± 0.09	-16.55 ± 0.07	5.94 ± 0.29	400	HDS
HD 105421	18.77 ± 0.04	-177.94 ± 0.05	-20.80 ± 0.07	7.64 ± 0.16	400	HDS
HD 105422	18.94 ± 0.05	-182.04 ± 0.06	-28.01 ± 0.06	...	400	HDS
HD 111484A	11.45 ± 0.05	-76.70 ± 0.10	-3.73 ± 0.06	-21.10 ± 0.20	400	HDS
HD 111484B	11.45 ± 0.44	-79.88 ± 0.08	-4.47 ± 0.06	-19.34 ± 0.31	300	HDS
HIP 70269A	23.86 ± 0.04	5.97 ± 0.08	-136.66 ± 0.07	-32.39 ± 0.16	400	HDS
HIP 70269B	23.77 ± 0.04	10.88 ± 0.07	-133.74 ± 0.06	-33.06 ± 0.16	400	HDS
HIP 70386A	26.29 ± 0.10	65.59 ± 0.15	-0.868 ± 0.11	-0.05 ± 0.92	400	HDS
HIP 70386B	26.54 ± 0.10	66.19 ± 0.13	0.60 ± 0.12	...	350	HDS

(This table is available in machine-readable form.)

possible (e.g., Meléndez et al. 2009; Bedell et al. 2014, 2018; Liu et al. 2014; Teske et al. 2016; Spina et al. 2018). In fact, when studying samples of twin stars, most of the systematic uncertainties that plague chemical abundance analyses are so similar among stars in the same binary pair that a strict differential line-by-line analysis cancels them out. Also NLTE effects have been found negligible for all the elements considered by our analysis of solar twin stars (Meléndez et al. 2012; Nissen 2015; Melendez et al. 2016; Spina et al. 2016), and so no NLTE corrections were required. This leaves the observational noise as the main source of error. Thus, error bars can be made very small simply by acquiring very high-quality spectra (i.e., a resolving power $R \geq 60,000$ and signal-to-noise ratio $S/N \geq 300$).

Eight binary systems were observed by the Ultraviolet and Visual Echelle Spectrograph (UVES; Dekker et al. 2000) on the Very Large Telescope of the European Southern Observatory.¹ The observations have been performed with a resolving power $R \sim 85,000$ and a wavelength coverage between 330 and 680 nm, though the DIC-1 (390+580). Another six pairs have been observed with the High Dispersion Spectrograph (HDS; Noguchi et al. 2002) on the Subaru telescope.² For the latter we have used a $R \sim 80,000$ and the Yc standard setup which covers the 439–705 nm spectral range. Thanks to the brightness

of our targets ($V \leq 9.3$ mag), we achieved an S/N ranging from 300 to 400 pixel⁻¹ at 600 nm, with a median of 350 pixel⁻¹. Solar spectra have been acquired both with UVES (S/N ~ 350) and HDS (S/N ~ 400) using the same instrument configurations described above.

All spectra have been normalized and Doppler-shifted using IRAF's `continuum` and `dopcor` tasks. Equivalent widths (EWs) of the atomic and molecular transitions reported in Meléndez et al. (2014) and listed in Table 2 have been measured with `Stellar diff`.³ This code allows the user to select one or more spectral windows for the continuum setting around each line of interest. Ideally, these windows coincide with regions devoid of other absorption lines. We employed the same window settings to calculate continuum levels and fit the lines of interest with Gaussian profiles in every spectrum. Therefore, the same assumptions have to be taken in the choice of the local continuum around the lines of interest. This is expected to minimize the effects of an imperfect spectral normalization or unresolved features in the continuum that can lead to larger errors in the differential abundances (Bedell et al. 2014). Furthermore, `Stellar diff` is able to identify points affected by hot pixels or cosmic rays and remove them from the calculation of the continuum. The code delivers the EW of each line of interest along with its uncertainty.

¹ Data was used from ESO program ID 0100.C-0090.

² Data was used from proposal ID o18123.

³ `Stellar diff` is a Python code publicly available at <https://github.com/andycasey/stellardiff>.

Table 2
Equivalent Width Measurements

Wavelength (Å)	Species	E.P. (eV)	Log gf	Sun (UVES) (mÅ)	BD+132311A (mÅ)	...
4365.896	26.0	2.990	-2.250	51.6	28.6	...
4389.245	26.0	0.052	-4.583	71.3	46.6	...
4445.471	26.0	0.087	-5.441	38.9
4950.106	26.0	3.417	-1.560	76.2	50.8	...
4994.129	26.0	0.915	-3.080	104.5	83.3	...
5044.211	26.0	2.851	-2.058	72.1	47.9	...
5054.642	26.0	3.640	-1.921	39.8	18.0	...
5127.359	26.0	0.915	-3.307	97.4	76.3	...
5127.679	26.0	0.052	-6.125	19.3
...

(This table is available in its entirety in machine-readable form.)

Table 3
Stellar Parameters

Star	T_{eff} (K)	log g (dex)	[Fe/H] (dex)	ξ (km s ⁻¹)
BD+132311A	6275 ± 27	4.117 ± 0.05	-0.224 ± 0.02	1.67 ± 0.05
BD+132311B	6295 ± 28	4.135 ± 0.06	-0.225 ± 0.02	1.54 ± 0.06
HIP 34407	5988 ± 8	4.378 ± 0.03	-0.335 ± 0.01	1.36 ± 0.02
HIP 34426	6047 ± 15	4.36 ± 0.03	-0.506 ± 0.02	1.57 ± 0.04
HIP 39409A	5620 ± 5	4.512 ± 0.02	0.044 ± 0.01	0.98 ± 0.02
HIP 39409B	5587 ± 6	4.477 ± 0.02	0.035 ± 0.01	0.95 ± 0.02
HIP 44858	5996 ± 12	4.507 ± 0.02	-0.324 ± 0.01	1.22 ± 0.02
HIP 44862	5595 ± 10	4.508 ± 0.03	-0.307 ± 0.01	1.21 ± 0.02
HIP 47836	6072 ± 11	4.407 ± 0.03	-0.310 ± 0.01	1.42 ± 0.03
HIP 47839	6149 ± 12	4.402 ± 0.04	-0.306 ± 0.01	1.5 ± 0.04
HIP 49520A	5915 ± 10	4.523 ± 0.02	-0.182 ± 0.01	1.13 ± 0.03
HIP 49520B	5846 ± 8	4.522 ± 0.02	-0.196 ± 0.01	1.06 ± 0.03
HIP 58298A	6171 ± 18	4.292 ± 0.04	-0.46 ± 0.01	1.79 ± 0.05
HIP 58298B	6177 ± 18	4.323 ± 0.05	-0.455 ± 0.01	1.82 ± 0.05
HR 4443	6216 ± 21	4.21 ± 0.05	0.017 ± 0.01	1.59 ± 0.04
HR 4444	6201 ± 19	4.183 ± 0.04	-0.028 ± 0.01	1.61 ± 0.03
HD 98744	6195 ± 21	3.975 ± 0.07	-0.309 ± 0.01	1.78 ± 0.05
HD 98745	6223 ± 31	4.301 ± 0.09	-0.228 ± 0.02	1.62 ± 0.04
HD 103431	5515 ± 6	4.445 ± 0.03	-0.158 ± 0.01	0.85 ± 0.02
HD 103432	5644 ± 7	4.497 ± 0.02	-0.13 ± 0.005	0.89 ± 0.01
HD 105421	6265 ± 13	4.49 ± 0.03	-0.096 ± 0.01	1.47 ± 0.02
HD 105422	6014 ± 15	4.497 ± 0.03	-0.139 ± 0.01	1.19 ± 0.02
HD 111484A	6249 ± 15	4.463 ± 0.04	0.104 ± 0.01	1.42 ± 0.02
HD 111484B	6243 ± 14	4.405 ± 0.04	0.125 ± 0.01	1.4 ± 0.02
HIP 70269A	5968 ± 11	4.385 ± 0.03	-0.23 ± 0.01	1.24 ± 0.02
HIP 70269B	5986 ± 9	4.403 ± 0.04	-0.24 ± 0.01	1.26 ± 0.03
HIP 70386A	6117 ± 18	4.507 ± 0.04	-0.043 ± 0.01	1.45 ± 0.03
HIP 70386B	5982 ± 11	4.508 ± 0.03	-0.066 ± 0.01	1.21 ± 0.02

(This table is available in machine-readable form.)

The iron EW measurements are processed by the qoyllurquipu (q2) code (Ramírez et al. 2014) that performs a line-by-line differential analysis relative to the solar spectrum and automatically estimates the stellar parameters (effective temperature T_{eff} , surface gravity log g , metallicity [Fe/H], and microturbulence ξ) by iteratively searching for the three equilibria: excitation, ionization, and the trend between the iron abundances and the reduced equivalent width. We assumed the nominal solar parameters, $T_{\text{eff}} = 5777$ K, log $g = 4.44$ dex, [Fe/H] = 0.00 dex, and $\xi = 1.00$ km s⁻¹ (Cox 2000). The iterations are executed with a series of steps starting from a set of initial parameters and employing the Kurucz (ATLAS9) grid of model atmospheres (Castelli & Kurucz 2004). In each step the

abundances are estimated using MOOG (version 2014, Sneden 1973). The errors associated with the stellar parameters are then evaluated by the code. This takes into account the dependence between the parameters in the fulfillment of the three equilibrium conditions (Epstein et al. 2010). We first run q2 adopting the solar parameters as a first guess for each star. After q2 has converged to a set of stellar parameters, the differential abundances relative to the Sun for the following elements are calculated: C I, CH, NH, Na I, Mg I, Al I, Si I, S I, Ca I, Sc II, Ti I, Ti II, V I, Cr I, Cr II, Mn I, Fe I, Fe II, Co I, Ni I, Cu I, Zn I, Y II, Zr II, and Ba II. Through the blends driver in MOOG and adopting the line list from the Kurucz database, the q2 code corrected the abundances of V, Mn, Co, Cu, and Y for hyperfine

Table 4
Differential Abundances Relative to the Sun

Star	[C I/H] (dex)	[CH/H] (dex)	[NH/H] (dex)	[O I/H] (dex)	[Na I/H] (dex)	...
BD+132311A	-0.17 ± 0.02 (3)	-0.23 ± 0.04 (1)	-0.05 ± 0.04 (1)	-0.022 ± 0.008 (1)	-0.25 ± 0.02 (3)	...
BD+132311B	-0.19 ± 0.03 (3)	-0.27 ± 0.05 (1)	-0.18 ± 0.05 (1)	0.01 ± 0.013 (1)	-0.37 ± 0.09 (3)	...
HIP 34407	-0.337 ± 0.017 (3)	-0.468 ± 0.009 (4)	-0.62 ± 0.15 (2)	-0.040 ± 0.007 (1)	-0.356 ± 0.019 (3)	...
HIP 34426	-0.330 ± 0.019 (3)	-0.53 ± 0.02 (4)	-0.55 ± 0.02 (1)	-0.102 ± 0.016 (1)	-0.503 ± 0.008 (3)	...
HIP 39409A	-0.055 ± 0.018 (3)	-0.023 ± 0.006 (4)	-0.05 ± 0.03 (2)	0.017 ± 0.006 (1)	-0.012 ± 0.003 (3)	...
HIP 39409B	-0.02 ± 0.06 (3)	-0.032 ± 0.009 (4)	-0.046 ± 0.015 (2)	0.027 ± 0.008 (1)	-0.012 ± 0.006 (3)	...
HIP 44858	-0.337 ± 0.017 (3)	-0.388 ± 0.016 (4)	-0.43 ± 0.11 (2)	...	-0.395 ± 0.019 (3)	...
HIP 44862	-0.32 ± 0.03 (3)	-0.386 ± 0.014 (4)	-0.41 ± 0.13 (2)	...	-0.383 ± 0.008 (3)	...
HIP 47836	-0.235 ± 0.013 (3)	-0.322 ± 0.015 (4)	-0.32 ± 0.08 (2)	0.000 ± 0.012 (1)	-0.302 ± 0.007 (3)	...
HIP 47839	-0.25 ± 0.03 (3)	-0.289 ± 0.017 (4)	-0.29 ± 0.11 (2)	0.021 ± 0.014 (1)	-0.28 ± 0.02 (3)	...
HIP 49520A	-0.228 ± 0.015 (3)	-0.235 ± 0.016 (3)	-0.29 ± 0.11 (2)	-0.079 ± 0.0017 (1)	-0.266 ± 0.015 (3)	...
...

Note. The number in brackets is the number of lines measured.

(This table is available in its entirety in machine-readable form.)

Table 5
Differential Abundances within Each Pair

Star1	Star 2	[C I/H] (dex)	[CH/H] (dex)	[NH/H] (dex)	[O I/H] (dex)	[Na I/H] (dex)	...
BD+132311A	BD+132311B	-0.02 ± 0.03 (3)	-0.03 ± 0.06 (1)	-0.12 ± 0.06 (1)	-0.01 ± 0.03 (1)	-0.13 ± 0.08 (3)	...
HIP 34407	HIP 34426	0.01 ± 0.03 (3)	-0.06 ± 0.02 (4)	-0.09 ± 0.03 (1)	-0.06 ± 0.03 (1)	-0.15 ± 0.02 (3)	...
HIP 39409A	HIP 39409B	0.05 ± 0.05 (3)	-0.008 ± 0.011 (4)	0.01 ± 0.02 (2)	0.010 ± 0.010 (1)	-0.001 ± 0.005 (3)	...
HIP 44858	HIP 44862	0.01 ± 0.02 (3)	0.00 ± 0.02 (4)	0.03 ± 0.02 (2)	...	0.009 ± 0.014 (3)	...
HIP 47836	HIP 47839	-0.01 ± 0.03 (3)	0.03 ± 0.02 (4)	0.03 ± 0.04 (2)	0.02 ± 0.02 (1)	0.03 ± 0.03 (3)	...
HIP 49520A	HIP 49520B	0.005 ± 0.016 (3)	-0.01 ± 0.02 (3)	-0.01 ± 0.04 (2)	-0.02 ± 0.02 (1)	-0.021 ± 0.015 (3)	...
HIP 58298A	HIP 58298B	0.00 ± 0.02 (2)	0.01 ± 0.04 (4)	-0.01 ± 0.04 (1)	-0.02 ± 0.02 (1)	-0.02 ± 0.04 (3)	...
HR 4443	HR 4444	-0.04 ± 0.05 (3)	-0.01 ± 0.03 (1)	0.02 ± 0.04 (1)	...	-0.01 ± 0.02 (2)	...
HD 98744	HD 98745	0.00 ± 0.04 (4)	0.06 ± 0.02 (3)	...
...

Note. The number in brackets is the number of lines measured.

(This table is available in its entirety in machine-readable form.)

splitting effects, by using the HFS components in the input line list. For each element, we performed a 3σ clipping on the abundances yielded by each EW measurement. This allowed us to remove the EW measurements affected by telluric lines or other unresolved blendings with adjacent lines. A second run of q2 using the restricted list of EW measurements yielded the stellar parameters listed in Table 3. Atmospheric T_{eff} values range from 5515 to 6295 K, while $\log g$ values range within 3.975–4.523 dex. All pairs are composed of twin stars.

With these final parameters, we repeated the calculation of the differential abundances relative to the Sun. The resulting abundances are listed in Table 4, together with their uncertainties and the number of lines used for the abundance determinations. The error budget associated with each elemental abundance has been obtained by summing in quadrature the standard error of the mean among the lines, and the propagated effects of the uncertainties on the stellar parameters. The typical precision that we achieved in individual stellar Fe I abundances is 0.01 dex. We also determined the differential abundances within each pair which are listed in Table 5.

The forbidden oxygen line at 6300.3 Å has been used to derive [O/H] for eight stars in our sample. The other stars either had too small of an [O I] line sunk in the spectral noise or were contaminated by O₂ telluric lines. The measurement of

this line requires particular care as it is small (typically 3–6 mÅ) and it is blended by a Ni line with nearly the same wavelength (Allende Prieto et al. 2001). Thus, we have followed a procedure already tested by Nissen (2015). Namely, (i) using Iraf’s `splot` task we measured the EW of [O I]+Ni line and its uncertainty by assuming different local continuum levels; (ii) through MOOG’s `ewfind` task and [Ni/H] abundances in Table 4, we have calculated the EW contribution of the Ni line and its uncertainty; (iii) we have subtracted the Ni contribution from the measured EW in order to estimate the EW of the [O I] line along with its uncertainty; (iv) using the [O I] EW and the parameters listed in Table 3, we calculated the [O/H] and its uncertainty. The oxygen differential abundances are also listed in Tables 4 and 5.

The differential abundances within each pair are plotted in Figure 1 as a function of the condensation temperature.

3. Results

In Table 6 we report the reduced chi-square value χ_{red}^2 of the pairs, which is defined as

$$\chi_{\text{red}}^2 = \frac{1}{N-1} \sum_{i=1}^N \left(\frac{\Delta[X_i/H]}{\sigma_{X_i}} \right)^2, \quad (1)$$

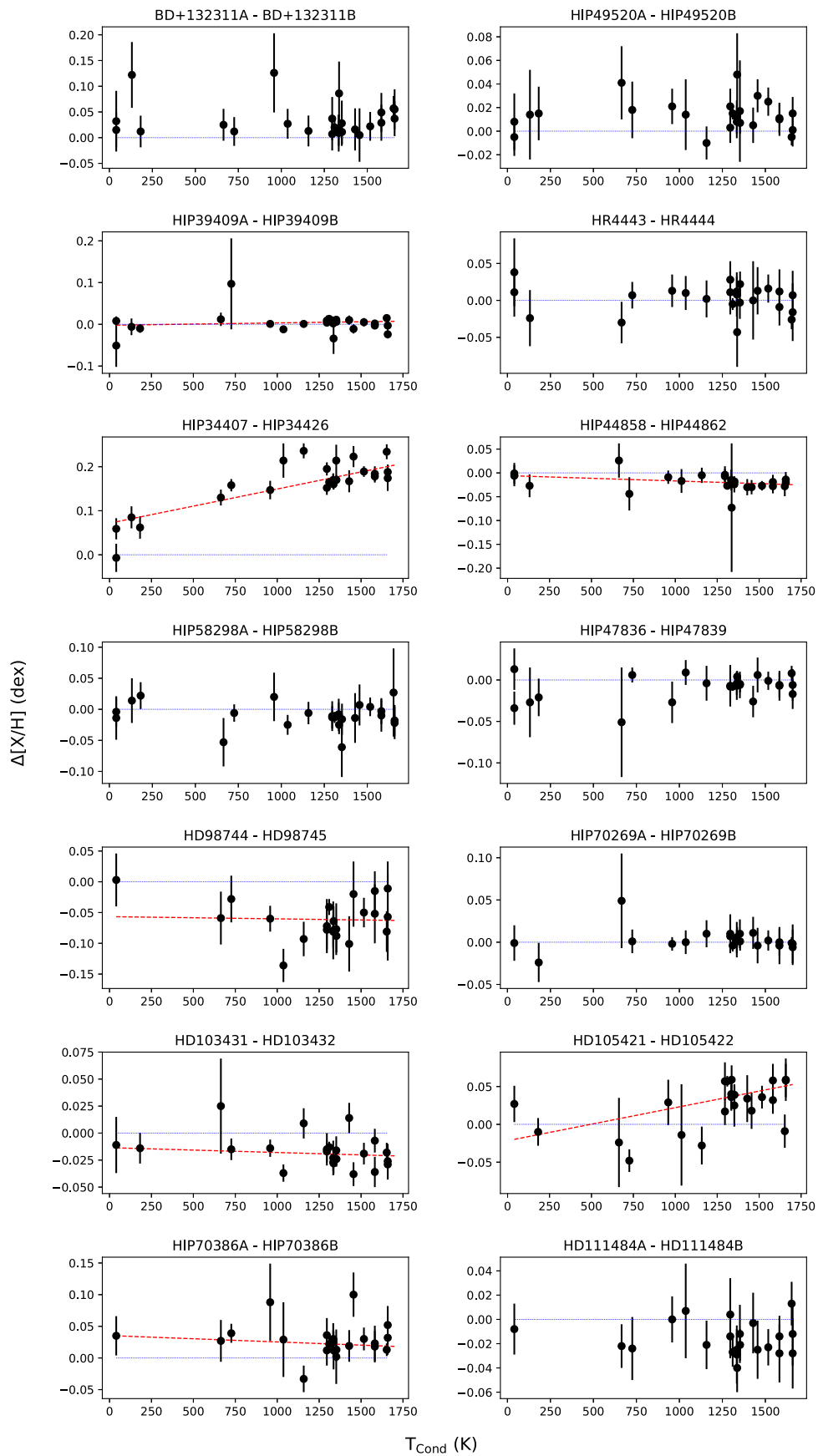


Figure 1. Each panel shows the differential abundances for a single system as a function of the condensation temperature. The red dashed lines are the results of the linear fitting of the $\Delta[X/H]-T_{\text{Cond}}$ distributions for the chemically anomalous pairs.

Table 6
Parameters for the Chemical Homogeneity Test

Binary System	χ_{red}^2	χ_{Survey}^2	σ_χ	$\Delta[X/H]$ vs. T_{Cond} Slope $10^{-6} \text{ dex K}^{-1}$
BD+132311A/BD+132311B	1.10	0.93	0.28	...
HIP 49520A/HIP 49520B	1.35	0.14	0.28	...
HIP 39409A/HIP 39409B	2.07	0.25	0.28	5.6 ± 5.9
HR 4443/HR 4444	0.57	0.14	0.28	...
HIP 34407/HIP 34426	118.99	12.07	0.28	77.6 ± 13.0
HIP 44858/HIP 44862	2.47	0.28	0.28	-11.2 ± 5.4
HIP 58298A/HIP 58298B	0.66	0.19	0.28	...
HIP 47836/HIP 47839	0.62	0.12	0.28	...
HD 98744/HD 98745	5.56	1.99	0.30	-3.6 ± 23.0
HIP 70269A/HIP 70269B	0.19	0.06	0.29	...
HD 103431/HD 103432	4.92	0.21	0.29	-4.5 ± 8.0
HD 105421/HD 105422	6.59	0.63	0.29	43.7 ± 15.4
HIP 70386A/HIP 70386B	1.95	0.62	0.30	-10.1 ± 12.5
HD 111484A/HD 111484B	1.28	0.18	0.30	...

(This table is available in machine-readable form.)

where $\Delta[X_i/H]$ is the differential abundance of the X_i^{th} -element within the pair, σ_{χ_i} its uncertainty, and N is the number of elements detected in the components of the pair. In order to assess if the pair is chemically anomalous or not, we can compare the χ_{red}^2 values with the value expected for the model where the pair is assumed to be chemically identical: $\chi_{\text{red}}^2 = 1$. However, as noted by Andrae et al. (2010), this value has an uncertainty $\sigma_\chi = 2/N$ which is given by the width of the χ -distribution due to the random noise of the data (which we can assume to be Gaussian). The σ_χ values are also listed in Table 6. Consequently, the six pairs of our sample with $\chi_{\text{red}}^2 > 1 + 3\sigma_\chi$ are all considered chemically anomalous.

The HIP 34407/HIP 34426 system has a χ_{red}^2 value of 118.99, indicating that the two stars differ considerably in chemical composition. Five other systems are chemically anomalous, although to a lesser extent. They are HIP 44858/HIP 44862, HD 98744/HD 98745, HD 103431/HD 103432, HD 105421/HD 105422, and HIP 70386A/HIP 70386B, which have χ_{red}^2 values equal to 2.47, 5.56, 4.92, 5.59, and 1.95 respectively. Therefore, out of the 14 pairs considered in this letter, 6 could render chemical tagging potentially inaccurate at our level of precision. However, assuming uncertainties of 0.05 dex for each element, which is a typical value for large spectroscopic surveys (e.g., Smiljanic et al. 2014; Buder et al. 2018), we calculated the χ_{Survey}^2 , also listed in Table 6. Based on this, only 2 pairs out of the 14 would result in being chemically inhomogeneous if targeted by a spectroscopic survey: HIP 34407/HIP 34426 and HD 98744/HD 98745.

A rocky planet falling into a star and polluting its atmosphere would result in a selective enhancement of refractory elements (Chambers 2001). Therefore, in order to verify if the chemical anomalies identified above could be attributed to planetary engulfment events, we have performed a linear fit of the differential abundances as a function of the condensation temperature. The resulting slopes are also listed in Table 6. Among the initial six chemically anomalous pairs, three have a slope that is consistent with being zero, while

another three pairs (i.e., HIP 44858/HIP 44862, HD 105421/HD 105422, and HIP 34407/HIP 34426) have a slope that is inconsistent with zero. However, it should be noted that most of the slopes listed in Table 6 are heavily driven by the differential abundances of the most volatile species, such as C, CH, O, and N (i.e., $T_{\text{Cond}} < 200$ K). In fact, the number of volatiles is much smaller than the number of refractory elements, as is visible in Figure 1. In addition, the chemical abundances of volatile elements are often more uncertain than those of refractories.

In the case of HIP 34407/HIP 34426, the chemical anomaly is extremely large compared to all the other pairs. The elements with an intermediate condensation temperature, such as Na, S, and Zn (i.e., $500 < T_{\text{Cond}} < 1000$ K) are well aligned by the $\Delta[X/H]-T_{\text{Cond}}$ relation plotted in Figure 1. This neat linear relation between elemental abundances and condensation temperature for this system may suggest that the anomaly was caused by a planetary engulfment event. Similar results were independently obtained by Ramirez et al. (2019).

Interestingly, the HIP 34407/HIP 34426 system was determined to be the most chemically inhomogeneous system found to date among other pairs in binary systems or clusters, that show similar trends between abundances and condensation temperature (Tucci Maia et al. 2014, 2019; Biazzo et al. 2015; Spina et al. 2015, 2018; Teske et al. 2015, 2016; Saffe et al. 2016, 2017; Oh et al. 2018). Its median differential abundance in the refractory elements is 0.19 dex. In addition, we note that the results from the HIP 34407/HIP 34426 system involve similar but not identical volatile elemental abundances. Out of the four most volatile species measured (i.e., $T_{\text{Cond}} < 200$ K), only one is consistent with zero, leading to the hypothesis that the slope is due to the engulfment of a gas giant. This is because such planets are capable of causing abundance changes in both volatiles (due to their gaseous outer layers) and refractories (due to their rocky cores and metallic inner layers). This hypothesis has been also proposed to explain a similar anomaly observed in the chemical composition of the 16 Cyg binary system (Tucci Maia et al. 2014, 2019).

4. Conclusions

The occurrence of chemically anomalous stars at the 0.01 dex precision level can be deduced from line-by-line differential analysis of twin stars in binary systems. Out of the 14 systems measured using UVES and HDS, 6 were found to exhibit chemical inhomogeneities (i.e., $\chi_{\text{red}}^2 > 1 + 3\sigma_\chi$), rendering chemical tagging on these systems inaccurate. However, only two pairs were chemically inhomogeneous at the precision level typical of large spectroscopic surveys (i.e., 0.05 dex).

Of special note is that the HIP 34407/HIP 34426 system was determined to be the most chemically inhomogeneous system found to date. For this pair, the trend between differential abundances and condensation temperature is neat, and it may suggest that rocky material has polluted the atmosphere of HIP 34407. We speculated that the planet engulfed by the star was a giant gaseous planet, as HIP 34426 is also anomalously rich in the volatiles. The planet population around the stars of this pair is currently unknown. Follow-up observations are required to establish if the two stars also have two different architectures for their planetary systems. This is necessary to understand the origin of similar anomalies observed within other stellar associations (Tucci Maia et al. 2014, 2019; Biazzo et al. 2015; Spina et al. 2015, 2018; Teske et al. 2015, 2016; Saffe et al. 2016, 2017; Oh et al. 2018), where the stars richer in refractory elements could also be the ones with a more chaotic architecture of their planetary systems.

Finally, systems whose components have identical stellar parameters and chemical patterns were also observed, such as the HIP 58298A/HIP 58298B and HR 4443/HR 4444 systems. These systems are excellent laboratories to test if other quantities, such as the thickness of the convective zone, stellar rotation, and activity can differ (and to what extent) among stars with equal mass, age, and chemical composition.

We thank the many scientists and engineers who made the UVES and HDS observations possible. It is a pleasure to acknowledge M. Asplund, A.R. Casey, J. Meléndez, and D. Yong for helpful discussions. L.S. and A.I.K. acknowledge financial support from the Australian Research Council (Discovery Project 170100521).

Facilities: VLT(UVES), Subaru(HDS).

Software: qoyllur-quipu (Ramírez et al. 2014), MOOG (Snedden 1973), Stellar diff (<https://github.com/andycasey/stellardiff>).

ORCID iDs

Tushar Nagar  <https://orcid.org/0000-0002-2747-0497>

Lorenzo Spina  <https://orcid.org/0000-0002-9760-6249>

Amanda I. Karakas  <https://orcid.org/0000-0002-3625-6951>

References

- Allende Prieto, C., Lambert, D. L., & Asplund, M. 2001, *ApJL*, 556, L63
 Andrae, R., Schulze-Hartung, T., & Melchior, P. 2010, arXiv:1012.3754
 Bedell, M., Bean, J. L., Meléndez, J., et al. 2018, *ApJ*, 865, 68
 Bedell, M., Meléndez, J., Bean, J. L., et al. 2014, *ApJ*, 795, 23
 Biazzo, K., Gratton, R., Desidera, S., et al. 2015, *A&A*, 583, A135
 Buder, S., Asplund, M., Duong, L., et al. 2018, *MNRAS*, 478, A4513
 Castelli, F., & Kurucz, R. L. 2004, in *IAU Symp. 210, Modelling of Stellar Atmospheres*, ed. N. Piskunov, W. W. Weiss, & D. F. Gray (San Francisco, CA: ASP), A20
 Chambers, J. 2018, *ApJ*, 865, 30
 Chambers, J. E. 2001, *Icar*, 152, 205
 Chambers, J. E. 2010, *ApJ*, 724, 92
 Cox, A. N. 2000, in *Allen's Astrophysical Quantities*, ed. A. N. Cox (Berlin: Springer)
 Dekker, H., D'Odorico, S., Kaufer, A., Delabre, B., & Kotzłowski, H. 2000, *Proc. SPIE*, 4008, 534
 Desidera, S., Gratton, R. G., Scuderi, S., et al. 2004, *A&A*, 420, 683
 Epstein, C. R., Johnson, J. A., Dong, S., et al. 2010, *ApJ*, 709, 447
 Freeman, K., & Bland-Hawthorn, J. 2002, *ARA&A*, 40, 487
 Fuhrmann, K., & Chini, R. 2015, *ApJ*, 809, 107
 Gaia Collaboration, Brown, A. G. A., Vallenari, A., et al. 2018, *A&A*, 616, A1
 Kane, S. R., Ciardi, D. R., Gelino, D. M., & von Braun, K. 2012, *MNRAS*, 425, 757
 Kenyon, S. J., & Bromley, B. C. 2016, *ApJ*, 817, 51
 Kunitomo, M., Guillot, T., Ida, S., & Takeuchi, T. 2018, *A&A*, 618, A132
 Liu, F., Asplund, M., Ramirez, I., Yong, D., & Melendez, J. 2014, *MNRAS: Letters*, 442, L51
 Liu, F., Yong, D., Asplund, M., et al. 2018, *A&A*, 614, A138
 Martín, E. L., Basri, G., Pavlenko, Y., & Lyubchik, Y. 2002, *ApJ*, 579, 437
 Martinez, M., Stone, N. C., & Metzger, B. D. 2019, *MNRAS*, 489, 5119
 Meléndez, J., Asplund, M., Gustafsson, B., & Yong, D. 2009, *ApJL*, 704, L66
 Melendez, J., Bedell, M., Bean, J. L., et al. 2016, *A&A*, 597, A34
 Meléndez, J., Bergemann, M., Cohen, J. G., et al. 2012, *A&A*, 543, A29
 Meléndez, J., Ramírez, I., Karakas, A. I., et al. 2014, *ApJ*, 791, 14
 Mróz, P., Ryu, Y. H., Skowron, J., et al. 2018, *AJ*, 155, 121
 Naoz, S., Farr, W. M., Lithwick, Y., Rasio, F. A., & Teysandier, J. 2011, *Natur*, 473, 187
 Nissen, P. E. 2015, *A&A*, 579, A52
 Noguchi, K., Aoki, W., Kawamoto, S., et al. 2002, *PASJ*, 54, 855
 Oh, S., Price-Whelan, A. M., Brewer, J. M., et al. 2018, *ApJ*, 854, 138
 Ramirez, I., Khanal, S., Lichon, S. J., et al. 2019, *MNRAS*, 490, 2448
 Ramírez, I., Meléndez, J., & Asplund, M. 2014, *A&A*, 561, A7
 Raymond, S. N., Izidoro, A., & Morbidelli, A. 2018, arXiv:1812.01033
 Saffe, C., Flores, M., Jaque Arancibia, M., Buccino, A., & Jofré, E. 2016, *A&A*, 588, A81
 Saffe, C., Jofré, E., Martioli, E., et al. 2017, *A&A*, 604, L4
 Smiljanic, R., Korn, A. J., Bergemann, M., et al. 2014, *A&A*, 570, A122
 Sneden, C. 1973, *ApJ*, 184, 839
 Spina, L., Meléndez, J., Karakas, A. I., et al. 2018, *MNRAS*, 474, 2580
 Spina, L., Meléndez, J., & Ramírez, I. 2016, *A&A*, 585, A152
 Spina, L., Palla, F., Randich, S., et al. 2015, *A&A*, 582, L6
 Teske, J. K., Ghezzi, L., Cunha, K., et al. 2015, *ApJL*, 801, L10
 Teske, J. K., Khanal, S., & Ramírez, I. 2016, *ApJ*, 819, 19
 Teske, J. K., Shectman, S. A., Vogt, S. S., et al. 2016, *AJ*, 152, 167
 Tucci Maia, M., Meléndez, J., Lorenzo-Oliveira, D., Spina, L., & Jofré, P. 2019, *A&A*, 628, A126
 Tucci Maia, M., Meléndez, J., & Ramírez, I. 2014, *ApJL*, 790, L25
 Winn, J. N., & Fabrycky, D. C. 2015, *ARA&A*, 53, 409
 Yana Galarza, J., Meléndez, J., Ramírez, I., et al. 2016, *A&A*, 589, A17